Hindawi
Structural Control and Health Monitoring
Volume 2023, Article ID 9756226, 17 pages
https://doi.org/10.1155/2023/9756226

Research Article

Optimal Design and Dynamic Analysis of a New Quasi-Zero-Stiffness Isolation Device

Tao Liu, Aiqun Li, and Hengyuan Zhang

Department of Civil Engineering, Southeast University, Nanjing 211189, China

Correspondence should be addressed to Aiqun Li; aiqunli@seu.edu.cn

Received 4 November 2022; Revised 9 April 2023; Accepted 28 June 2023; Published 18 July 2023

Academic Editor: Łukasz Jankowski

Compared with the linear isolation system, the quasi-zero-stiffness (QZS) nonlinear isolation system has the characteristics of high static stiffness and low dynamic stiffness, which has better low-frequency vibration isolation performance. However, most of the existing QZS isolators only consider the quasi-zero-stiffness characteristic at the static equilibrium position achieved by the parallel connection of positive and negative stiffness structures. To optimize the isolation performance of the QZS system, a new isolation device based on the parallel connection of oblique springs and vertical springs was proposed. The device can not only achieve quasi-zero-stiffness at the static equilibrium position but also expand the interval of quasi-zero-stiffness through parameter optimization design to optimize the stiffness characteristics of the QZS system, thus effectively improving the vibration isolation performance. The QZS nonlinear systems with the optimal parameters were analyzed dynamically, and the nonlinear motion equations were approximately solved based on the fifth-order polynomials fitted by the restoring force curves. A prototype was further designed and fabricated to compare and analyze the vibration isolation performance of the QZS system and the equivalent linear system through a shaking table test.

1. Introduction

A quasi-zero-stiffness isolation system is generally composed of the positive stiffness mechanism for bearing the main load and the negative stiffness mechanism for offsetting the positive stiffness around the static equilibrium position. The high-static-low-dynamic stiffness characteristics make the QZS system have a wider isolation frequency band and better isolation performance than the linear stiffness system [1]. A great deal of research and applications have been carried out on QZS isolators with different structures, such as multispring structures [2–5], special spring structures [6–9], origami structures [10–12], buckling beam structures [13–16], geometric nonlinear structures [17–19], magnetic structures [20–22], bioinspired structures [23–25], and other types of structures [26–30]. All these QZS systems can be effectively used in low-frequency vibration isolation.

Carrella et al. and Kovacic et al. first studied the quasi-zero-stiffness system proposed by Molyneux [31] and simplified the model into a third-order approximate Duffing equation. They further analyzed the static problems [32], force and displacement transmissibility [33, 34], and its application in rotor isolation [35]. The dynamic analysis is mainly based on the first-order approximate solution obtained by the harmonic balance method. It is considered that the isolation performance of the QZS isolator can be reflected only when the downward jump frequency of the QZS system is less than the corresponding resonance frequency of the linear system. Neild and Wagg [36–38] studied the amplitude-frequency response characteristics of the above QZS isolator through a fifth-order polynomial function. QZS systems are often limited in practical engineering applications, one of the important reasons being that they only form near the static equilibrium position region, which means that the optimal performance of the QZS system is limited to a small excitation amplitude. Considering that some vibration will produce a larger displacement response, how to achieve quasi-zero-stiffness and expand the interval of quasi-zero-stiffness to optimize the stiffness

characteristics of the system and effectively improve the vibration isolation performance has become a key problem to be solved [39–41].

This paper focuses on the optimal parameter design of the proposed device which uses quasi-zero-stiffness around the static equilibrium position, by comparing the values of dynamic stiffness in the entire compression stroke range of the device, and the innovations are described as follows:

(1) In contrast to the conventional QZS system, a three-spring QZS system was proposed by Molyneux, and the physical and geometric parameters of the proposed device can be adjusted and controlled through a slide-link connection system and mechanical assembly, allowing for more flexible adjustment and use in practical engineering.

(2) The proposed device can improve the vibration isolation performance by expanding the quasi-zero-stiffness range through parameter optimization design. The nonlinear dynamics analysis shows that the proposed QZS system has a smaller vibration isolation starting frequency and a larger vibration isolation frequency range than the conventional QZS system and the equivalent linear system for vibration isolation, and the performance improves more significantly as the excitation amplitude decreases.

(3) In this paper, a new QZS isolation device based on the parallel connection of oblique springs and vertical springs has been developed, fabricated, and tested by the authors. The displacement transmissibility of the quasi-zero-stiffness vibration isolation system and the equivalent linear vibration isolation system were compared and analyzed by the shaking table test, which verified the good low-frequency vibration isolation performance of the device.

2. Isolation Device Description and Static Analysis

The device consists of three parts: the bearing plate and connecting rod; the vertical and oblique spring systems; and upper and bottom limit plates, vertical rails, and sliders. The three main components are integrated through a central connection block, enabling the device to achieve quasi-zero-stiffness at the static equilibrium position through the parametric adjustment of the spring stiffness characteristics, as shown in Figure 1.

The negative stiffness system consists of eight symmetrically arranged precompressed inclined springs. By adjusting the distance between the upper and bottom limit plates or the distance between the four vertical rails, the precompression coefficients of the inclined spring can be easily adjusted, thus changing the stiffness characteristics of the negative stiffness system. Similarly, by replacing different vertical springs, the vertical stiffness system can be controlled according to different needs. Then the two systems can be connected in parallel to achieve the adjustable quasi-zero-stiffness characteristics.

The inclined springs of the device are supported internally by a piston rod to maintain stability in compression, a damping fluid can be added inside the piston rod, and the springs can be replaced by other stiffness elements with better compressibility and elasticity to meet the actual needs in different projects. The geometric parameters of the QZS device and the physical parameters of the spring system are shown in Figure 2, with the device in a static equilibrium position, which is the force state of the device under the design mass load.

The isolation device introduces the following parameters: linear stiffness coefficient k_2 for the vertical spring; linear stiffness coefficient k_1 and softening cubic stiffness coefficient k_3 for the precompressed inclined spring; precompression coefficient δ and vertical projection length h for the oblique spring system; the displacement parameter x of the isolated object from the static equilibrium position; and distance e of the upper and lower threaded caps from the central connection block.

Note that $\sqrt{a^2+b^2+h^2}$ does not represent the original length of the spring, as the precompression δ is not zero. The relationship between the vertical applied force f and the resulting displacement x can be given as follows.

When $-h < x < h$

$$
\begin{aligned}
f = {} & 4k_2x + \frac{1+\operatorname{sgn}(x+e)(x-e)}{2}\operatorname{sgn}[\operatorname{abs}(x+e)(x-e)]\times \\
& \cdot\left\{4k_1(h-x)\left(\frac{\sqrt{a^2+b^2+h^2}+\delta}{\sqrt{a^2+b^2+(h-x)^2}}-1\right)-4k_1(h+x)\left(\frac{\sqrt{a^2+b^2+h^2}+\delta}{\sqrt{a^2+b^2+(h+x)^2}}-1\right)\right. \\
& +4k_3\frac{h-x}{\sqrt{a^2+b^2+(h-x)^2}}\left(\sqrt{a^2+b^2+(h-x)^2}-\sqrt{a^2+b^2+h^2}-\delta\right)^3 \\
& \left.-4k_3\frac{h+x}{\sqrt{a^2+b^2+(h+x)^2}}\left(\sqrt{a^2+b^2+(h+x)^2}-\sqrt{a^2+b^2+h^2}-\delta\right)^3\right.,
\end{aligned}
\tag{1}
$$

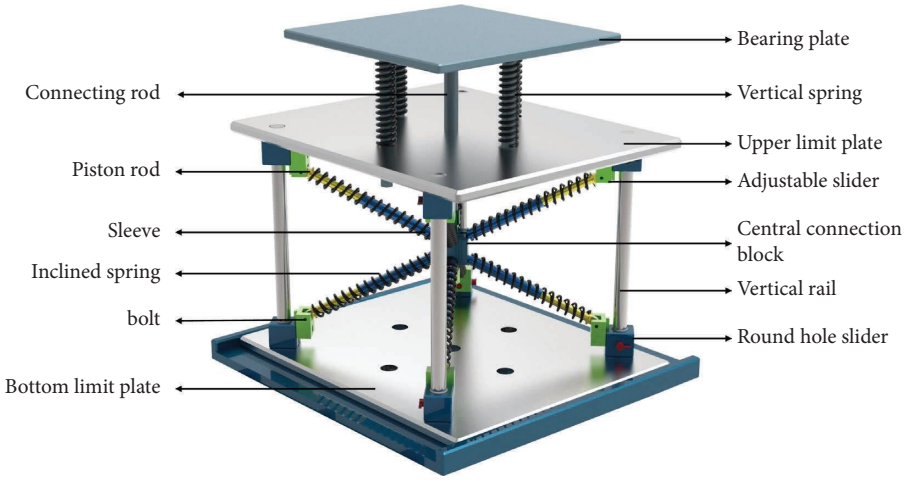

Figure 1: View of quasi-zero-stiffness isolation device.

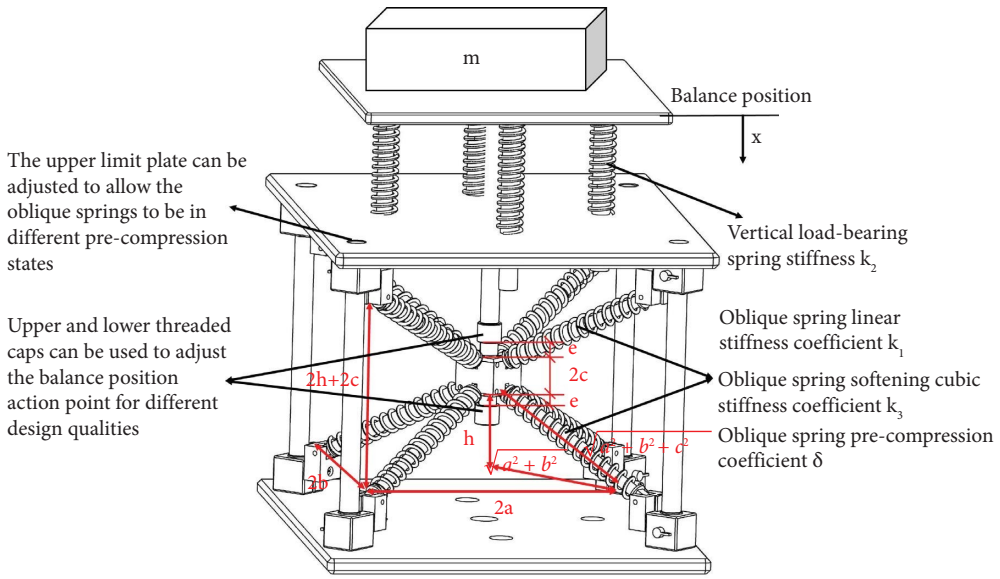

Figure 2: The geometric parameters of the QZS device and the physical parameters of the spring systems.

where $\mathrm{sgn}(x)$ is the symbolic function and $\mathrm{abs}(x)$ is the absolute value function, further introducing the dimensionless parameter: $\tilde{f} = f/(4k_2\sqrt{a^2+b^2+h^2})$, $\tilde{x} = x/\sqrt{a^2+b^2+h^2}$, $\tilde{h} = h/\sqrt{a^2+b^2+h^2}$, $\tilde{\delta} = \delta/\sqrt{a^2+b^2+h^2}$, $\alpha = k_1/k_2$, and $\beta = k_3(a^2+b^2+c^2)/k_2$, and the force expression of the nondimensional form can be derived as follows:

$$\tilde{f} = \tilde{x} + \frac{1+\mathrm{sgn}(\tilde{x}+\tilde{e})(\tilde{x}-\tilde{e})}{2}\mathrm{sgn}\left[\mathrm{abs}(\tilde{x}+\tilde{e})(\tilde{x}-\tilde{e})\right] \times\left\{\alpha\psi_1(\Delta_1-1) - \beta\psi_1 P_1{}^2(\Delta_1-1)^3 - \alpha\psi_2(\Delta_2-1) + \beta\psi_2 P_2{}^2(\Delta_2-1)^3\right\}. \tag{2}$$

The expressions of each of these simplified parameters are as follows: $\psi_1 = \tilde{h} - \tilde{x}, \psi_2 = \tilde{h} + \tilde{x}, P_1 = \sqrt{\tilde{x}^2 - 2\tilde{h}\tilde{x} + 1}$, $P_2 = \sqrt{\tilde{x}^2 + 2\tilde{h}\tilde{x} + 1}, \Delta_1 = (1 + \tilde{\delta})/P_1$ and $\Delta_2 = (1 + \tilde{\delta})/P_2$

The nondimensional stiffness $\tilde{K}$ can be further derived as follows:

$$\begin{aligned}\tilde{K} = 1 + \frac{1 + \operatorname{sgn}(\tilde{x} + \tilde{e})(\tilde{x} - \tilde{e})}{2} \operatorname{sgn}[\operatorname{abs}(\tilde{x} + \tilde{e})(\tilde{x} - \tilde{e})] \\ \times \alpha\left[1 - \left(1 - \tilde{h}^2\right)\frac{\Delta_1}{{P_1}^2}\right] - \beta(\Delta_1 - 1)^2\left[(1 - \Delta_1)\left(3{\psi_1}^2 + 1 - \tilde{h}^2\right) + 3{\psi_1}^2\Delta_1\right] \\ + \alpha\left[1 - \left(1 - \tilde{h}^2\right)\frac{\Delta_2}{{P_2}^2}\right] - \beta(\Delta_2 - 1)^2\left[(1 - \Delta_2)\left(3{\psi_2}^2 + 1 - \tilde{h}^2\right) + 3{\psi_2}^2\Delta_2\right].\end{aligned} \tag{3}$$

It can be seen from the Figure 2 that when $e = 0$, the upper and bottom compression stroke of the device is the vertical projection length h of the oblique spring, and the force analysis of the system when $e \neq 0$ is not considered for the time being.

If $\tilde{K} = 0$ is specified at $\tilde{x} = 0$ and $e = 0$, then the value of α and β can be obtained as follows:

$$\begin{aligned}1 + 2\alpha\left\{1 - \left(1 - \tilde{h}^2\right)(1 + \tilde{\delta})\right\} \\ - 2\beta\tilde{\delta}^2\left\{3\tilde{h}^2 - \tilde{\delta}\left(1 - \tilde{h}^2\right)\right\} = 0,\end{aligned} \tag{4}$$

$$\beta = \frac{1 + 2\alpha\left\{1 - \left(1 - \tilde{h}^2\right)(1 + \tilde{\delta})\right\}}{2\tilde{\delta}^2\left\{3\tilde{h}^2 - \tilde{\delta}\left(1 - \tilde{h}^2\right)\right\}}, \tag{5}$$

when $\beta > 0$, the oblique spring is soft, and when $\beta < 0$, the oblique spring is hard. In order to ensure that the oblique springs on both sides are not in a state of tension, the individual parameters of the springs also need to satisfy the following: $\sqrt{a^2 + b^2 + h^2} + \delta \geq \sqrt{a^2 + b^2 + (2h)^2}$. Considering the small value of $\tilde{h}^2$, further simplification is given in the following equation:

$$\tilde{\delta} \geq \sqrt{1 + 3\tilde{h}^2} - 1 \approx \frac{3\tilde{h}^2}{2}. \tag{6}$$

Substituting equation (6) into equation (5) and making $\alpha > 0$ and $\beta > 0$ lead to $0 < \tilde{h} < 0.577$. Therefore, when considering the precompression of the oblique spring system, the value of $\tilde{h}$ is best chosen between 0 and 0.5 in order to ensure that the mechanical properties of the QZS isolation system are meaningful.

3. Optimum Parameter Design of the QZS Device

In order to optimize and extend the quasi-zero-stiffness interval of the device, it is necessary to keep the dimensionless stiffness $\tilde{K}$-surface as close to the zero axis as possible at the static equilibrium position ($\tilde{x} = 0$), while ensuring the positive stiffness characteristics of the device over the entire range of compression strokes. When $e = 0$, bringing equation (5) into equation (3) yields

$$\begin{aligned}\tilde{K} = 1 + \alpha \times \left\{2 - \left(1 - \tilde{h}^2\right)\frac{\Delta_1}{{P_1}^2} - \left(1 - \tilde{h}^2\right)\frac{\Delta_2}{{P_2}^2}\right\} - \frac{1 + 2\alpha\left[1 - \left(1 - \tilde{h}^2\right)(1 + \tilde{\delta})\right]}{2\tilde{\delta}^2\left[3\tilde{h}^2 - \tilde{\delta}\left(1 - \tilde{h}^2\right)\right]} \\ \times \left\{(\Delta_1 - 1)^2\left[3{\psi_1}^2 + \left(\tilde{h}^2 - 1\right)(\Delta_1 - 1)\right] + (\Delta_2 - 1)^2\left[3{\psi_2}^2 + \left(\tilde{h}^2 - 1\right)(\Delta_2 - 1)\right]\right\}.\end{aligned} \tag{7}$$

Figure 3 shows the three-dimensional surface diagram of the dimensionless stiffness $\tilde{K}$ with parameters $\tilde{x}$ and $\tilde{\delta}$ for $\tilde{h} = 0.2$ and $\alpha = 1$, as well as the $\tilde{K} - \tilde{x}$ diagram and the $\tilde{K} - \tilde{\delta}$ diagram for different viewpoints. It can be seen from Figure 3 that the abrupt change in the value of dimensionless stiffness $\tilde{K}$ is at $\tilde{\delta} = 3\tilde{h}^2/(1 - \tilde{h}^2)$ and $\tilde{\delta} = 0$. This is due to the fact that the conditions $\tilde{\delta} \neq 3\tilde{h}^2/(1 - \tilde{h}^2)$ and $\tilde{\delta} \neq 0$ need to be satisfied in equation (5); otherwise, the expression is meaningless.

Considering that the stiffness ratio α needs to be greater than 0, a three-dimensional surface plot of the stiffness ratio α with parameters β and $\tilde{\delta}$ can be made for $\tilde{h} = 0.1$, as well as $\alpha - \beta$ diagram and $\alpha - \tilde{\delta}$ diagram from different viewpoints, as shown in Figure 4. It can be seen that the sudden change of the stiffness ratio α is at $\tilde{\delta} = \tilde{h}^2/(1 - \tilde{h}^2)$. When $\tilde{h}^2/(1 - \tilde{h}^2) < \tilde{\delta} < 1$ and $0 < \beta < 8$, the stiffness ratio α of the QZS device is greater than 0. Note that the values of β and $\tilde{\delta}$ are taken only in consideration of the parameters that may be

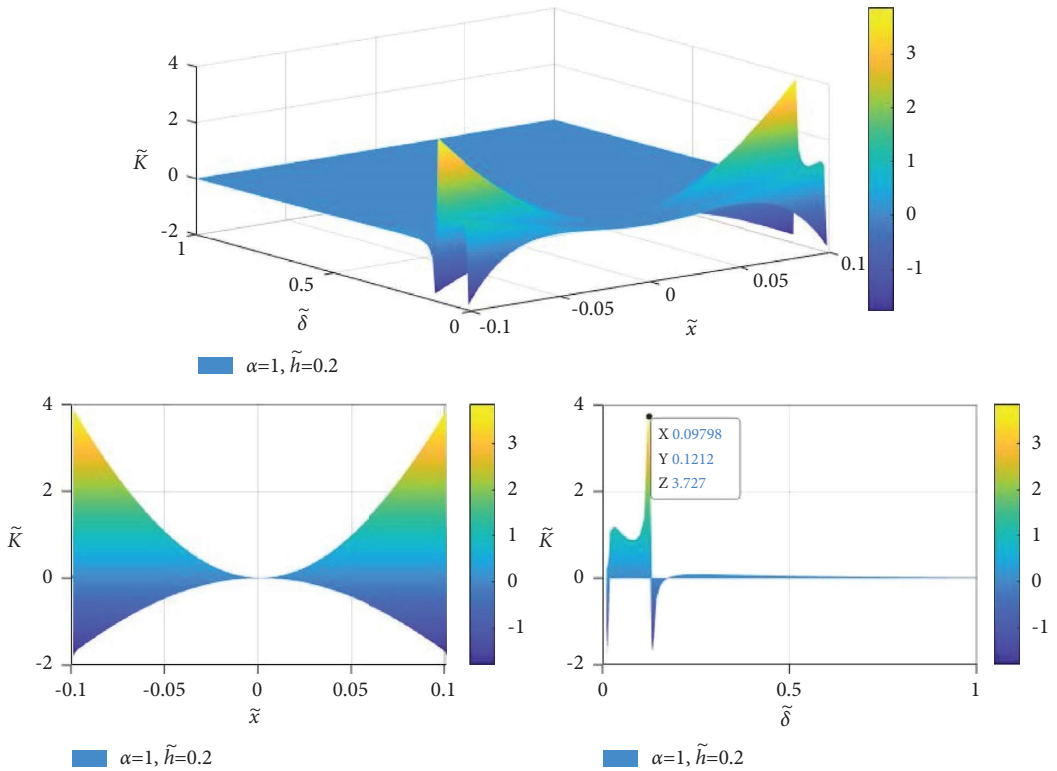

FIGURE 3: The three-dimensional surface diagram of the dimensionless stiffness $\widetilde{K}$ with parameters $\widetilde{x}$ and $\widetilde{\delta}$, as well as the $\widetilde{K}-\widetilde{x}$ diagram and the $\widetilde{K}-\widetilde{\delta}$ diagram $(\alpha = 1, \widetilde{h} = 0.2, \beta \neq 0)$.

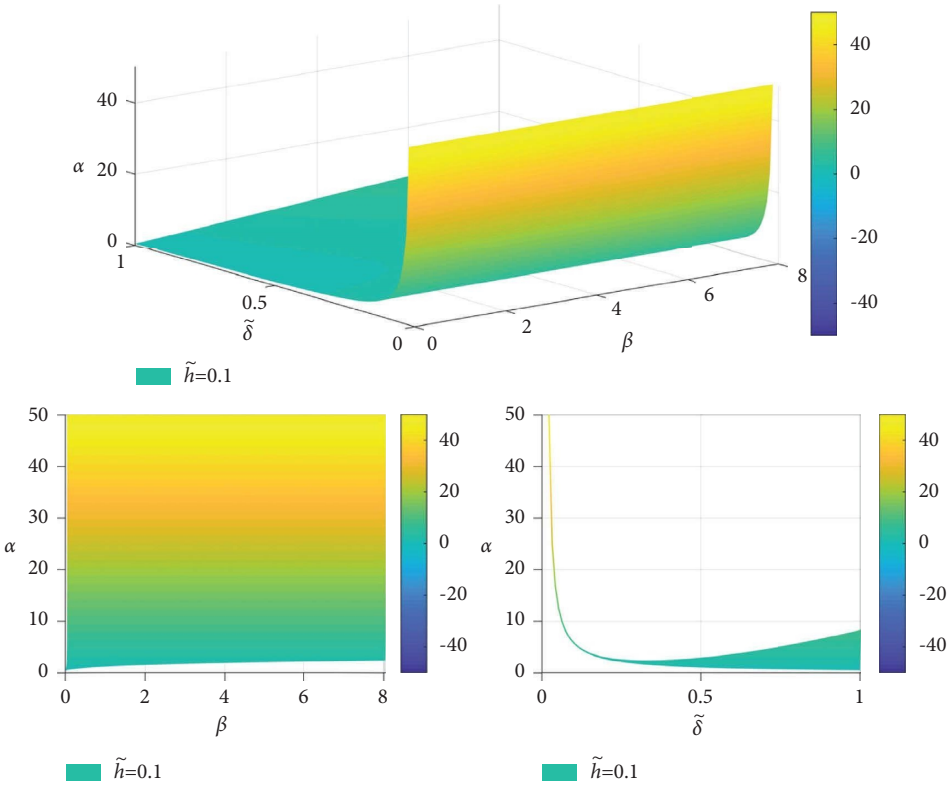

FIGURE 4: The three-dimensional surface diagram of the stiffness ratio α with parameters β and $\widetilde{\delta}$, as well as the $\alpha-\beta$ diagram and the $\alpha-\widetilde{\delta}$ diagram $(\widetilde{h} = 0.1, \beta \neq 0)$.

taken in practical engineering applications and do not imply that the stiffness ratio α is greater than 0 only when β and $\tilde{\delta}$ are taken in this interval.

Figures 5 and 6 show the $\alpha-\beta$ view and $\alpha-\tilde{\delta}$ view when $\tilde{h}=0.2\sim0.5$. It can be seen that the stiffness ratio α of the QZS device is greater than 0 for $\tilde{h}=0.2\sim0.4$, $\tilde{h}^2/(1-\tilde{h}^2)<\tilde{\delta}<1$, $0<\beta<8$ and for $\tilde{h}=0.5$, $\tilde{h}^2/(1-\tilde{h}^2)<\tilde{\delta}<1$, $0<\beta<4$. From Figures 4 to 6, it can be seen that when the pre-compression factor $\tilde{\delta}>\tilde{h}^2/(1-\tilde{h}^2)$ and the softening cubic stiffness factor $0<\beta<4$, the stiffness ratio $\alpha>0$ can meet the needs of the actual project.

According to the selection range of parameters, the three-dimensional surface plots of its dimensionless stiffness $\tilde{K}$ with parameters $\tilde{x}$ and $\tilde{\delta}$ for different values $\tilde{h}=0.1$, $\tilde{\delta}\in[0.04,5]$; $\tilde{h}=0.2$, $\tilde{\delta}\in[0.08,5]$; $\tilde{h}=0.3$, $\tilde{\delta}\in[0.14,5]$; and $\tilde{h}=0.4$, $\tilde{\delta}\in[0.22,5]$ when the softening cubic stiffness coefficient $\beta=0.05$, 0.25, 0.5, and 0.75 are shown in Figure 7. It can be seen that for different values of β and $\tilde{h}$, the concavity and convexity of the 3D surface are transformed at a certain value of $\tilde{\delta}$. When the value of $\tilde{\delta}$ is in the small range, the dimensionless stiffness $\tilde{K}$ is a 3D concave surface, and when the value of $\tilde{\delta}$ is in the large range, the dimensionless stiffness $\tilde{K}$ is a 3D convex surface.

To see this property more clearly, the 3D surface plots of the dimensionless stiffness $\tilde{K}$ with parameters $\tilde{x}$ and $\tilde{\delta}$ are made by taking $\beta=0.5$, $\tilde{h}=0.1$, and $\tilde{\delta}\in[0.04,5]$, as well as the $\tilde{K}-\tilde{x}$ diagram and the $\tilde{K}-\tilde{\delta}$ diagram views from different viewpoints, as shown in Figure 8. It can be seen from Figures 7 and 8 that the dimensionless stiffness $\tilde{K}$ surface produces a shift in concavity at a critical value of $\tilde{\delta}$. Therefore, the critical parameter $\tilde{\delta}$ value is found by solving for $\tilde{K}''(0)=0$.

By deriving equation (7), the first-order derivative $\tilde{K}'$ and the second-order derivative $\tilde{K}''$ can be further derived as follows:

$$\begin{aligned}\tilde{K}' &= -3\alpha\times\left(1-\tilde{h}^2\right)(1+\tilde{\delta})\left(\frac{\psi_1}{P_1{}^5}-\frac{\psi_2}{P_2{}^5}\right)\\ &\quad-3\beta\times\psi_1\left[2\psi_1{}^2\frac{\Delta_1(\Delta_1-1)}{P_1{}^2}+\left(\tilde{h}^2-1\right)\frac{\Delta_1(\Delta_1-1)^2}{P_1{}^2}-2(\Delta_1-1)^2\right]\\ &\quad-\psi_2\left[2\psi_2{}^2\frac{\Delta_2(\Delta_2-1)}{P_2{}^2}+\left(\tilde{h}^2-1\right)\frac{\Delta_2(\Delta_2-1)^2}{P_2{}^2}-2(\Delta_2-1)^2\right],\end{aligned}\tag{8}$$

$$\begin{aligned}\tilde{K}'' &= 3\alpha\times\left(1-\tilde{h}^2\right)(1+\tilde{\delta})\left(\frac{1}{P_1{}^5}+\frac{1}{P_2{}^5}-\frac{5\psi_1{}^2}{P_1{}^7}-\frac{5\psi_2{}^2}{P_2{}^7}\right)\\ &\quad-3\beta\times2(\Delta_1-1)^2-\frac{\Delta_1(\Delta_1-1)\left[\left(\tilde{h}^2-1\right)(\Delta_1-1)+10\psi_1{}^2\right]}{P_1{}^2}\\ &\quad+\frac{\psi_1{}^2\Delta_1(\Delta_1-1)\left[\left(\tilde{h}^2-1\right)(5\Delta_1-3)+8\psi_1{}^2\right]+2\psi_1{}^4\Delta_1}{P_1{}^4}\\ &\quad+2(\Delta_2-1)^2-\frac{\Delta_2(\Delta_2-1)\left[\left(\tilde{h}^2-1\right)(\Delta_2-1)+10\psi_2{}^2\right]}{P_2{}^2}\\ &\quad+\frac{\psi_1{}^2\Delta_2(\Delta_2-1)\left[\left(\tilde{h}^2-1\right)(5\Delta_2-3)+8\psi_2{}^2\right]+2\psi_2{}^4\Delta_2}{P_2{}^4}.\end{aligned}\tag{9}$$

By equation (9), the equation of $\tilde{K}''(0)=0$ can be obtained as equation (11), and the corresponding curves of the critical parameters $\tilde{\delta}$ and $\tilde{h}$ when $\tilde{K}''(0)=0$, $\beta=0.05$ can be made, as shown in Figure 9. It can be seen that when the parameter $\tilde{h}$ is small, the change of the critical parameter $\tilde{\delta}$ is also small, and when the parameter $\tilde{h}$ is large, the change of the critical parameter $\tilde{\delta}$ also increases, especially when $\tilde{h}>0.3$, the variation of the critical parameter $\tilde{\delta}$ increases sharply. For practical use, considering the limited compression coefficient $\tilde{\delta}$ of the spring, a smaller value of $\tilde{h}$ is chosen in the optimal parameter selection.

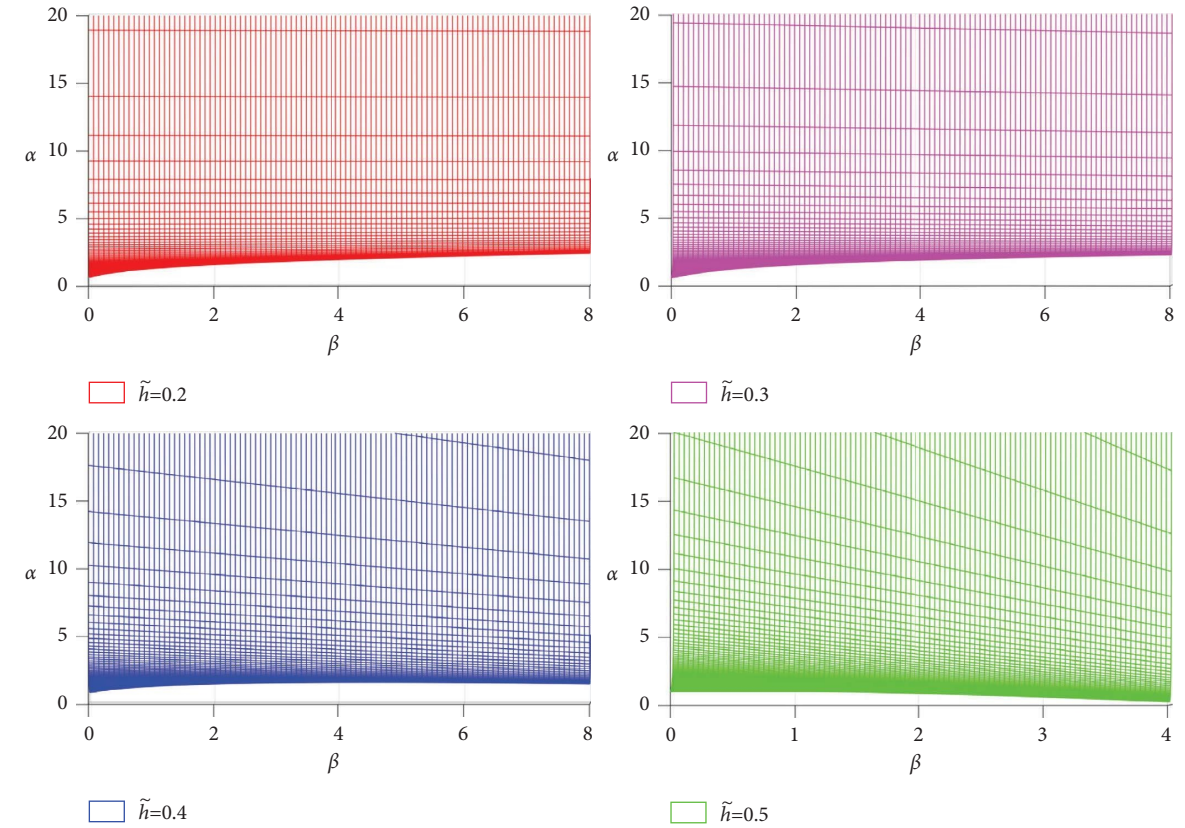

Figure 5: The $\alpha - \beta$ view when $\tilde{h} = 0.2 \sim 0.5$.

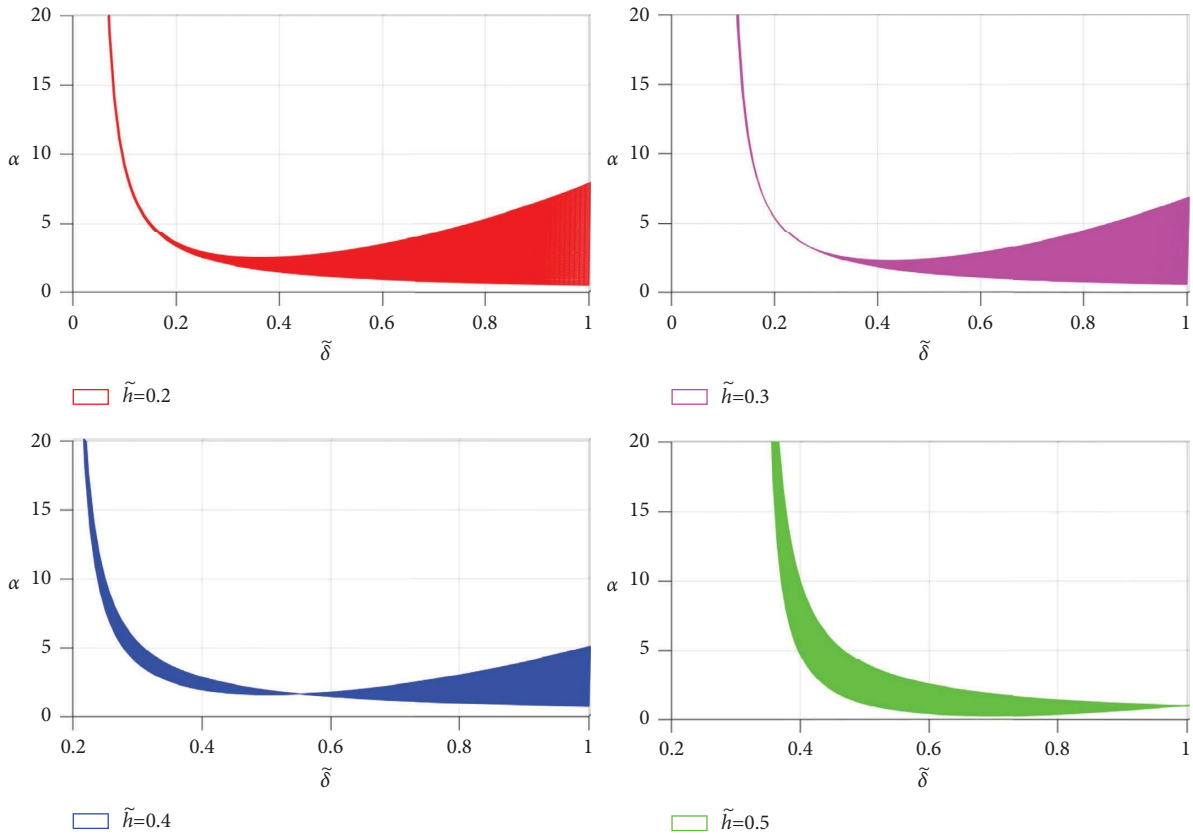

Figure 6: The $\alpha - \tilde{\delta}$ view when $\tilde{h} = 0.2 \sim 0.5$.

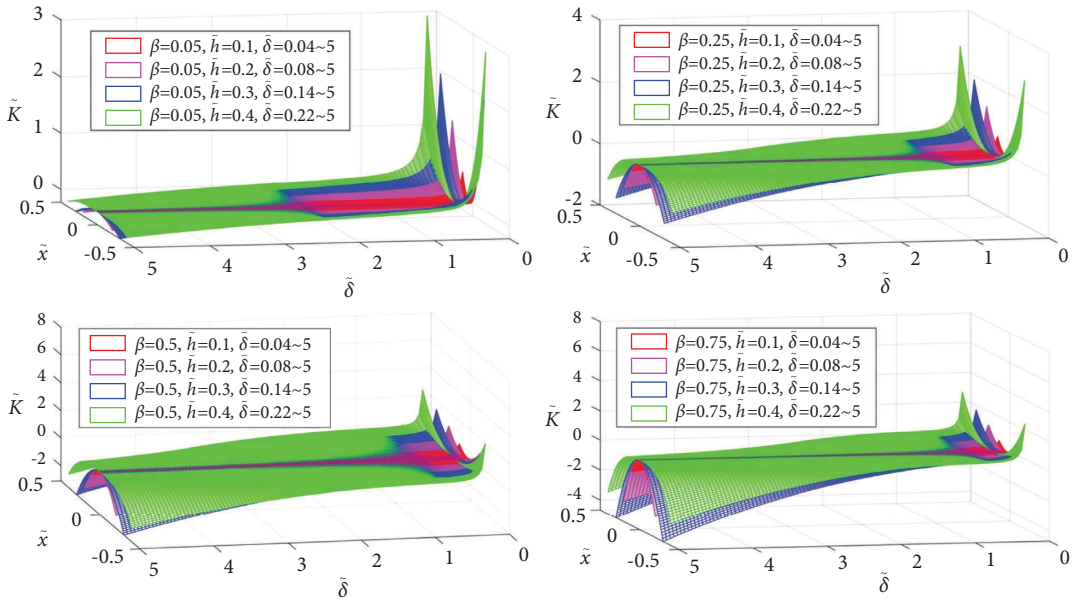

FIGURE 7: The three-dimensional surface diagram of the dimensionless stiffness $\tilde{K}$ with parameters $\tilde{x}$ and $\tilde{\delta}$ ($\tilde{h} = 0.1 \sim 0.4, \beta = 0.05, 0.25, 0.5,$ and 0.75).

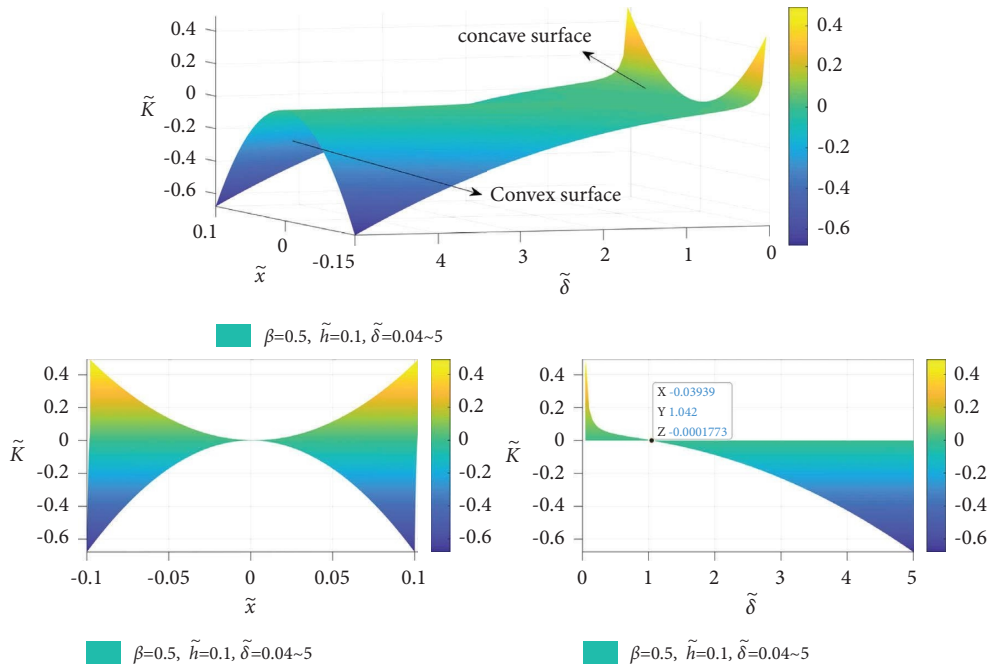

FIGURE 8: The three-dimensional surface diagram of the dimensionless stiffness $\tilde{K}$ with parameters $\tilde{x}$ and $\tilde{\delta}$, as well as the $\tilde{K} - \tilde{x}$ diagram and the $\tilde{K} - \tilde{\delta}$ diagram ($\tilde{h} = 0.1$ and $\beta = 0.5$).

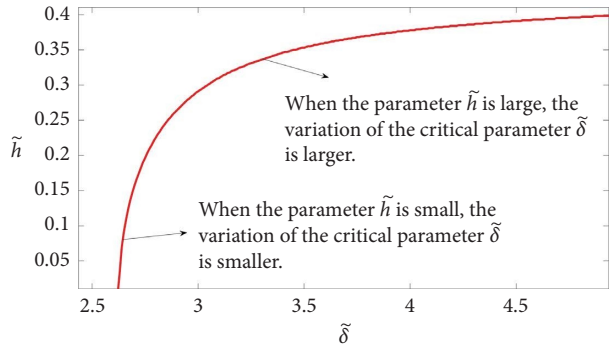

FIGURE 9: Correspondence curves of the critical parameter $\tilde{\delta}$ and $\tilde{h}$ when $\tilde{K}''(0) = 0$ and $\beta = 0.05$.

$$\alpha\left(1-\tilde{h}^2\right)\left(1-5\tilde{h}^2\right)(1+\tilde{\delta})-\frac{1+2\alpha\left[1-\left(1-\tilde{h}^2\right)(1+\tilde{\delta})\right]}{2\tilde{\delta}^2\left[3\tilde{h}^2-\tilde{\delta}\left(1-\tilde{h}^2\right)\right]} \times\left[\left(5\tilde{h}^4-6\tilde{h}^2+1\right)\tilde{\delta}^3+\left(15\tilde{h}^4-18\tilde{h}^2+3\right)\tilde{\delta}^2+\left(12\tilde{h}^4-12\tilde{h}^2\right)\tilde{\delta}+2\tilde{h}^4\right]=0, \tag{10}$$

$$\begin{aligned}\tilde{K}'''(x) = {} & 15\alpha\left(1-\tilde{h}^2\right)(1+\tilde{\delta})\left(\frac{3\psi_1}{{P_1}^7}-\frac{3\psi_2}{{P_2}^7}-\frac{7{\psi_1}^3}{{P_1}^9}+\frac{7{\psi_2}^3}{{P_2}^9}\right)-3\beta\times\psi_1\Delta_1 \\ & \times 24\frac{\Delta_1-1}{{P_1}^2}-\frac{\left(\tilde{h}^2-1\right)\left(15{\Delta_1}^2-24\Delta_1+9\right)+2{\psi_1}^4(36\Delta_1-31)+8}{{P_1}^4} \\ & +\frac{{\psi_1}^2\left[\left(\tilde{h}^2-1\right)\left(35{\Delta_1}^2-48\Delta_1+15\right)+2{\psi_1}^2(24\Delta_1-15)\right]}{{P_1}^6}-\psi_2\Delta_2 \\ & \times 24\frac{\Delta_2-1}{{P_2}^2}-\frac{\left(\tilde{h}^2-1\right)\left(15{\Delta_2}^2-24\Delta_2+9\right)+2{\psi_2}^4(36\Delta_2-31)+8}{{P_2}^4} \\ & +\frac{{\psi_2}^2\left[\left(\tilde{h}^2-1\right)\left(35{\Delta_2}^2-48\Delta_2+15\right)+2{\psi_2}^2(24\Delta_2-15)\right]}{{P_2}^6},\end{aligned} \tag{11}$$

$$\begin{aligned}\tilde{K}''''(x) = {} & -45\alpha\left(1-\tilde{h}^2\right)(1+\tilde{\delta})\left(\frac{1}{{P_1}^7}+\frac{1}{{P_2}^7}-\frac{14{\psi_1}^2}{{P_1}^9}-\frac{14{\psi_2}^2}{{P_2}^9}+\frac{21{\psi_1}^4}{{P_1}^{11}}+\frac{21{\psi_2}^4}{{P_2}^{11}}\right)-3\beta \\ & \times\Delta_1\frac{24(1-\Delta_1)}{{P_1}^2}+\frac{8+\left(\tilde{h}^2-1\right)\left(15{\Delta_1}^2-24\Delta_1+9\right)+24{\psi_1}^2(4\Delta_1-3)+10{\psi_1}^4(36\Delta_1-31)}{{P_1}^4} \\ & -\frac{6{\psi_1}^2\left(\tilde{h}^2-1\right)\left(35{\Delta_1}^2-48\Delta_1+15\right)+10{\psi_1}^4(24\Delta_1-15)+2{\psi_1}^6(216\Delta_1-55)+40{\psi_1}^2}{{P_1}^6} \\ & +\frac{3{\psi_1}^4\left(\tilde{h}^2-1\right)\left(35{\Delta_1}^2-32\Delta_1+5\right)+2{\psi_1}^6(48\Delta_1-15)}{{P_1}^8} \\ & +\frac{6{\psi_1}^4\left(\tilde{h}^2-1\right)\left(35{\Delta_1}^2-48\Delta_1+15\right)+12{\psi_1}^6(24\Delta_1-15)}{{P_1}^{10}}\end{aligned}$$

$$+\Delta_2\frac{24(1-\Delta_2)}{{P_2}^2}+\frac{8+\left(\tilde{h}^2-1\right)\left(15{\Delta_2}^2-24\Delta_2+9\right)+24{\psi_2}^2\left(4\Delta_2-3\right)+10{\psi_2}^4\left(36\Delta_2-31\right)}{{P_2}^4}$$
$$-\frac{6{\psi_2}^2\left(\tilde{h}^2-1\right)\left(35{\Delta_2}^2-48\Delta_2+15\right)+10{\psi_2}^4\left(24\Delta_2-15\right)+2{\psi_2}^6\left(216\Delta_2-55\right)+40{\psi_2}^2}{{P_2}^6}$$
$$+\frac{3{\psi_2}^4\left(\tilde{h}^2-1\right)\left(35{\Delta_2}^2-32\Delta_2+5\right)+2{\psi_2}^6\left(48\Delta_2-15\right)}{{P_2}^8}$$
$$+\frac{6{\psi_2}^4\left(\tilde{h}^2-1\right)\left(35{\Delta_2}^2-48\Delta_2+15\right)+12{\psi_2}^6\left(24\Delta_2-15\right)}{{P_2}^{10}}, \tag{12}$$

$$\begin{aligned}\tilde{K}''''(0)=&-90\alpha\times\left(1-\tilde{h}^2\right)(1+\tilde{\delta})\left(1-14\tilde{h}^2+21\tilde{h}^4\right)\\&-6\beta\times(1+\tilde{\delta})\left(315\tilde{h}^6-525\tilde{h}^4+225\tilde{h}^2-15\right)\tilde{\delta}^2\\&+\left(198\tilde{h}^6-258\tilde{h}^4+234\tilde{h}^2-30\right)\tilde{\delta}-112\tilde{h}^6-88\tilde{h}^4-4\tilde{h}^2+8,\end{aligned} \tag{13}$$

$$\begin{aligned}\tilde{f}=&-0.75\alpha\times\left(1-\tilde{h}^2\right)(1+\tilde{\delta})\left(1-14\tilde{h}^2+21\tilde{h}^4\right)\\&-0.05\beta\times(1+\tilde{\delta})\left(315\tilde{h}^6-525\tilde{h}^4+225\tilde{h}^2-15\right)\tilde{\delta}^2\\&+\left(198\tilde{h}^6-258\tilde{h}^4+234\tilde{h}^2-30\right)\tilde{\delta}-112\tilde{h}^6-88\tilde{h}^4-4\tilde{h}^2+8\tilde{x}^5+o\left(\tilde{x}^5\right)\\=&\chi\tilde{x}^5+o\left(\tilde{x}^5\right).\end{aligned} \tag{14}$$

From the correspondence between the values of the critical parameter $\tilde{\delta}$ and $\tilde{h}$ in Figure 10, the relationship between the nonlinear coefficients χ and the critical parameter $\tilde{\delta}$ and $\tilde{h}$ can be further obtained, as shown in Figure 10. It can be seen that for different values of β and critical parameters $\tilde{\delta}$ and $\tilde{h}$, the nonlinear coefficients χ show increasing and then decreasing characteristics, and when $\tilde{\delta}$ and $\tilde{h}$ are larger, the nonlinear coefficients χ are negative, which is not allowed to occur in practical applications.

When $\tilde{K}''(0)=0$, a further derivative of equation (10) is required in order to perform a Taylor series expansion of the dimensionless restoring force $\tilde{f}$. The third-order derivative $\tilde{K}'''$ and fourth-order derivative $\tilde{K}''''$ and $\tilde{K}''''(0)$ can be further derived, as shown in equations (12)–(14). Further combining equations (11) and (14), the dimensionless restoring force $\tilde{f}$ at $\tilde{x}=0$ can be expanded in a fifth-order Taylor series, as shown in equation (15).

In summary, when considering different softening cubic stiffness coefficients β, we can obtain four different sets of optimal parameters for the QZS device as follows: $\beta=0.05$, $\alpha=0.542$, $\tilde{h}=0.108$, $\tilde{\delta}=2.66$, $\chi=0.1640$; $\beta=0.25$, $\alpha=0.826$, $\tilde{h}=0.099$, $\tilde{\delta}=1.35$, $\chi=0.3076$; $\beta=0.5$, $\alpha=1.015$, $\tilde{h}=0.109$, $\tilde{\delta}=1.03$, and $\chi=0.4120$; and $\beta=0.75$, $\alpha=1.148$, $\tilde{h}=0.107$, $\tilde{\delta}=0.88$, and $\chi=0.4714$.

4. Dynamic Analysis of the QZS Device under Optimal Parameter

4.1. Comparison of Exact and Approximate Expressions. Figure 11 shows the comparison curves between the exact expression of the dimensionless restoring force $\tilde{f}$ and the fifth-order Taylor series expansion for four different sets of optimization parameters. It can be seen that the fifth-order Taylor series expansion fits poorly at the end of the compression stroke of the device, and the error between the approximate expression and the exact expression increases with the increase of the displacement $\tilde{x}$ of the QZS system. When $\beta=0.05$, the fifth-order Taylor series expansion fits best, and along with the increase of β, the fifth-order expansion fits gradually worse, and when the dimensionless displacement $\tilde{x}$ is less than 0.05, it fits well for different values of β.

4.2. Force and Displacement Transmissibility. Assuming that the device has viscous damping in the vertical direction, when a simple harmonic force excitation is applied to the isolated object or a displacement excitation is applied to the foundation, the equation of motion can be derived as

$$\begin{aligned}mx''(t)+cx'(t)+f&=F\cos\omega t,\\m\ddot{z}(t)+c\dot{z}(t)+f&=m\omega^2Z_e\cos\omega t,\end{aligned} \tag{15}$$

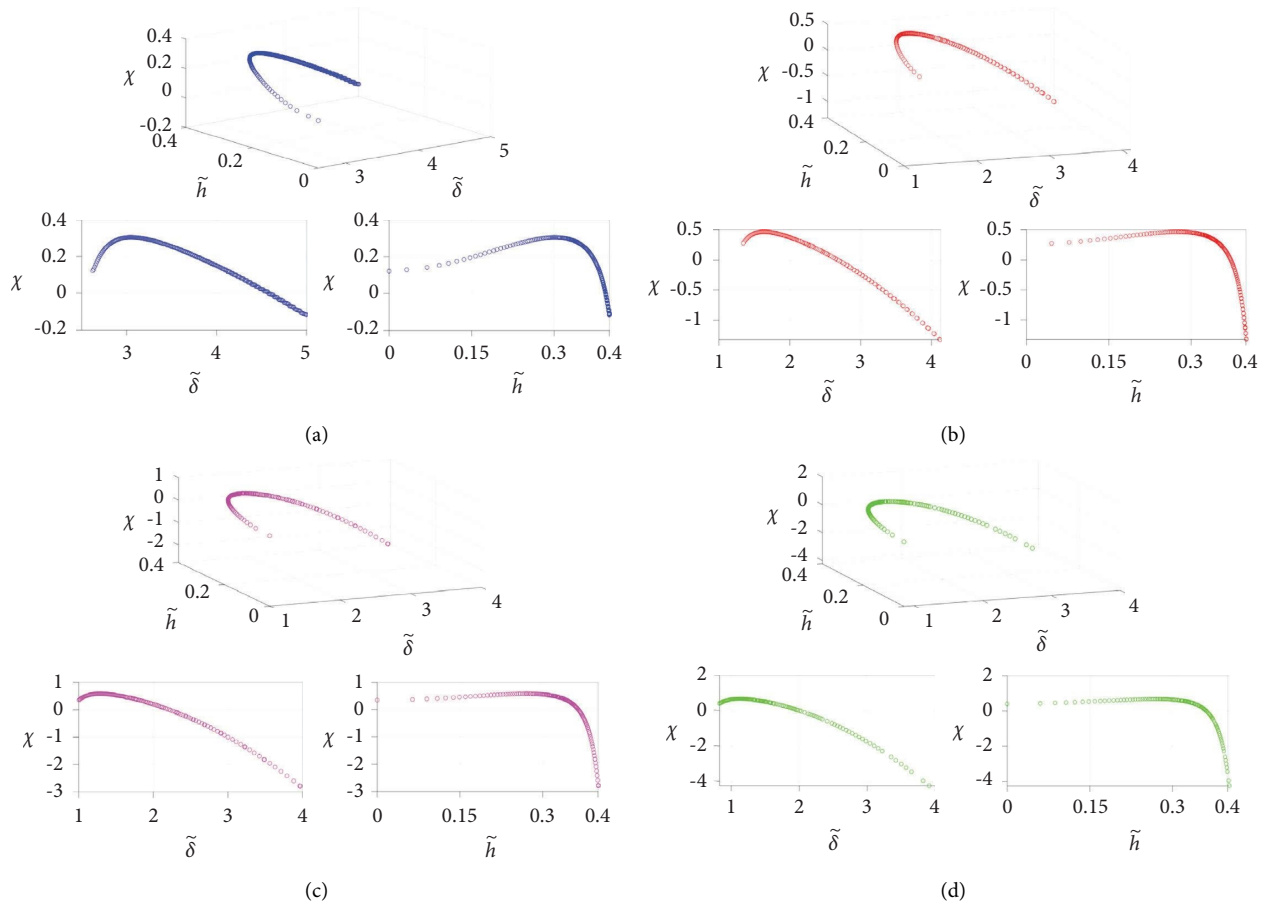

Figure 10: The relationship curve between the nonlinear coefficient χ and the values of critical parameters $\tilde{\delta}$ and $\tilde{h}$: (a) $\beta = 0.05$, (b) $\beta = 0.25$, (c) $\beta = 0.5$, and (d) $\beta = 0.75$.

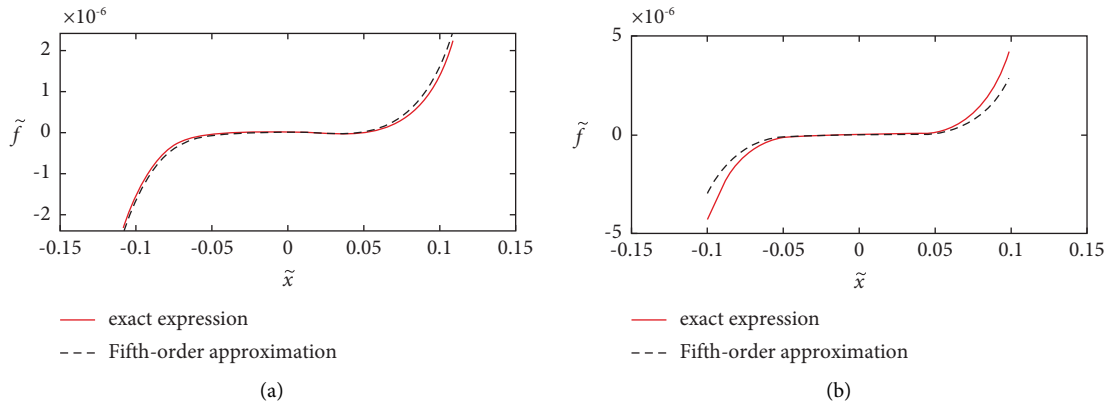

Figure 11: Continued.

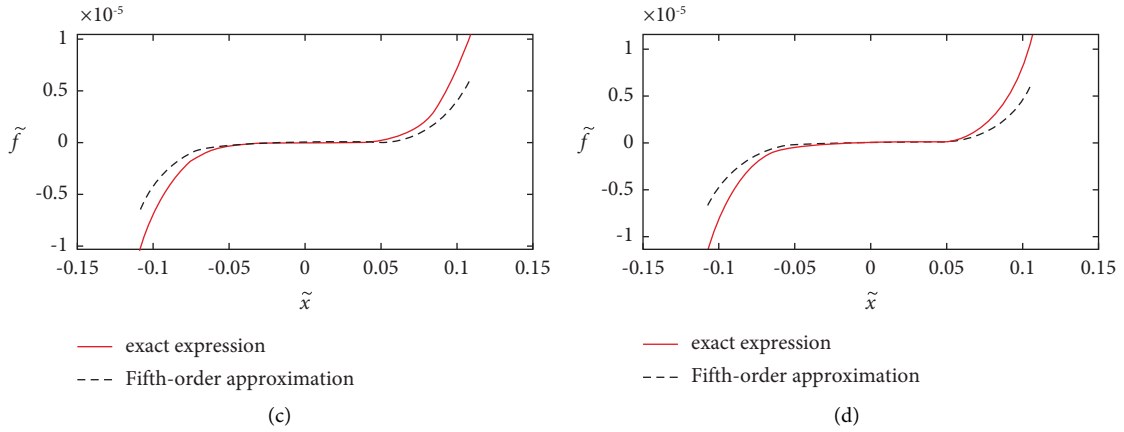

FIGURE 11: The dimensionless vertical force $\tilde{f}$ and fifth-order Taylor approximation expansion: (a) $\beta = 0.05$, $\alpha = 0.542$, $\tilde{h} = 0.108$, and $\tilde{\delta} = 2.66$, (b) $\beta = 0.25$, $\alpha = 0.826$, $\tilde{h} = 0.099$, $\tilde{\delta} = 1.35$, and $\chi = 0.3076$, (c) $\beta = 0.5$, $\alpha = 1.015$, $\tilde{h} = 0.109$, $\tilde{\delta} = 1.03$, and $\chi = 0.4120$, and (d) $\beta = 0.75$, $\alpha = 1.148$, $\tilde{h} = 0.107$, $\tilde{\delta} = 0.88$, and $\chi = 0.4714$.

By dimensionless processing: $\tilde{f} = f/(4k_2\sqrt{a^2+b^2+h^2})$, $\tilde{x} = x/\sqrt{a^2+b^2+h^2}$, $\tilde{F} = F/(k_2\sqrt{a^2+b^2+h^2})$, $\tilde{Z}_e = Z_e/\sqrt{a^2+b^2+h^2}$, $\tilde{z} = z/\sqrt{a^2+b^2+h^2}$, $\Omega = \omega/\omega_0$, ${\omega_0}^2 = k_2/m$, and $2\xi = c\omega_0/k_2$, the equations can be further derived as

$$\tilde{x}''(\tau) + 2\xi\tilde{x}'(\tau) + 4\chi\tilde{x}^5(\tau) = \tilde{F}\cos(\Omega\tau), \tag{16}$$

$$\tilde{z}''(\tau) + 2\xi\tilde{z}'(\tau) + 4\chi\tilde{z}^5(\tau) = \Omega^2\tilde{Z}_e\cos(\Omega\tau). \tag{17}$$

Assuming the so-called T-periodic solutions $\tilde{x}(\tau) = A\cos(\Omega\tau+\theta)$ and $\tilde{z}(\tau) = \tilde{Z}\cos(\Omega\tau+\theta)$, then applying the harmonic balance method to equations (16) and (17), the following equations can be derived as

$$\left(-\Omega^2 A + \frac{5}{2}\chi A^5\right)^2 + (-2\xi A\Omega)^2 = \tilde{F}^2, \tag{18}$$

$$\left(-\Omega^2\tilde{Z} + \frac{5}{2}\chi\tilde{Z}^5\right)^2 + (-2\xi\tilde{Z}\Omega)^2 = \Omega^4{\tilde{Z}_e}^2. \tag{19}$$

Note that the dimensionless force transmitted to the isolated structure by the QZS system is $\tilde{f}_t = 2\xi\tilde{x}'(\tau) + 4\chi\tilde{x}^5(\tau)$. Assuming $\tilde{f}_t = \tilde{F}_t\cos(\Omega\tau+\theta)$ and $\tilde{x}(\tau) = A\cos(\Omega\tau+\theta)$ and expanding $4\chi\tilde{x}^5(\tau)$ into Fourier series, it can be obtained as ${\tilde{F}_t}^2 = (5/2\chi A^5)^2 + (2\xi A\Omega)^2$. Combined with equation (19), the force transmissibility T_F can be further deduced as

$$T_F = \frac{\tilde{F}_t}{\tilde{F}} = \frac{|A|\sqrt{\left(5/2\chi A^4\right)^2 + (2\xi\Omega)^2}}{\tilde{F}}. \tag{20}$$

The conventional QZS system consists of a vertical spring connected at point O with two oblique springs, as shown in Figure 12 [33, 42]. The force transmissibility of conventional QZS system T_F was given in equation (21) where $\chi = 1.6459$ was used at $\beta = 0$. When considering $\beta = 0$, we can also obtain a set of optimal parameter for the QZS device from equation (2) as follows: $\alpha = 1$, $\tilde{h} = 0.447$, $\tilde{\delta} = 0.876$, and $\chi = 1.0805$

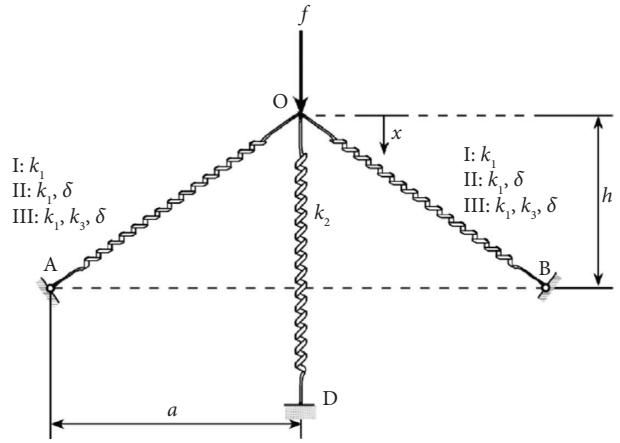

FIGURE 12: A three-spring model of a conventional QZS mechanism.

$$T_F = \frac{\tilde{F}_t}{\tilde{F}} = \frac{|A|\sqrt{\left(3/4\chi A^2\right)^2 + (2\xi\Omega)^2}}{\tilde{F}}. \tag{21}$$

Similarly combining equation (19), the relative displacement transmissibility $T_Z = \tilde{Z}/\tilde{Z}_e$ can be further derived as

$$\left(-\Omega^2 T_Z + \frac{5}{2}\chi{\tilde{Z}_e}^4 {T_Z}^5\right)^2 + \left(-2\xi T_Z\Omega\right)^2 = \Omega^4. \tag{22}$$

The relative displacement transmissibility of conventional QZS system T_{Z_tra} was given in equation (23) where $\tilde{Z}_e = 0.0449$ was used at $\beta = 0$ [42].

$$\left(-\Omega^2 T_Z + \frac{3}{4}\chi{\tilde{Z}_e}^2 {T_{Z\_tra}}^3\right)^2 + \left(-2\xi T_{Z\_tra}\Omega\right)^2 = \Omega^4. \tag{23}$$

Based on equations (18) and (20), the force transmissibility T_F of the QZS system and the equivalent linear system is plotted for the four different sets of optimal parameters, as shown in Figure 13. As can be seen from Figure 13, compared to the equivalent linear system, the

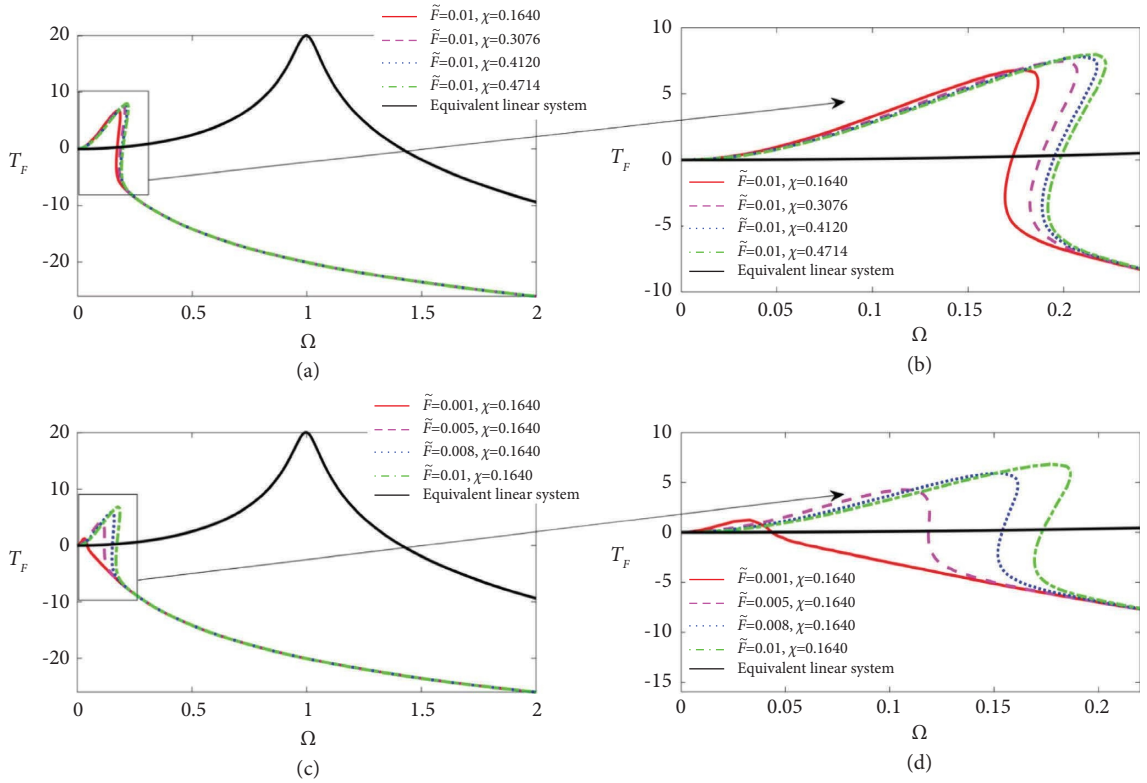

Figure 13: Force transmissibility of the QZS system and equivalent linear system with the damping coefficient of 0.05: (a) comparison of nonlinear systems with different optimal parameters when $\widetilde{F} = 0.01$, (b) partial enlargement of (a), (c) comparison of nonlinear systems with different values of $\widetilde{F}$ when $\chi = 0.1640$, and (d) partial enlargement of (c).

quasi-zero-stiffness system with optimal parameters has a wider isolation frequency range and a lower amplitude of vibration, which can isolate lower-frequency vibrations. For the QZS system, as the excitation amplitude $\widetilde{F}$ decreases or the nonlinear coefficients χ decreases, the maximum value of the force transmissibility and the corresponding resonant frequency decrease, resulting in better isolation performance compared to the equivalent linear system.

As shown in Figure 14, the force transmissibility of the proposed QZS system and the corresponding conventional QZS system are plotted for two amplitudes of force excitation based on equations (20) and (21). It is easy to find that the proposed QZS system has a lower amplitude, a smaller isolation start frequency, and a larger isolation frequency range compared with the conventional QZS system and equivalent linear system, and the isolation performance becomes better as the amplitude of force excitation decreases.

Based on equation (22), the relative transmissibility T_Z of the QZS system and the equivalent linear system is plotted for two different sets of parameters, as shown in Figure 15(a). One set of parameters is the optimal parameters when the nonlinear coefficient $\chi = 0.1640$, and the other one is the one for the QZS system when $\widetilde{h} = 0.1$ without considering the nonlinear coefficient β. It is worth noting from Figure 15(a) that when the nonlinear coefficient $\chi = 0.1640$, the maximum value of relative transmissibility under harmonic excitation conditions disappears, which gives the QZS system with optimal parameters better low-frequency vibration isolation performance than the QZS system without considering the nonlinear coefficient β and the equivalent linear system.

Figure 15(b) shows a comparison of the relative displacement transferability between the proposed QZS system and the corresponding conventional QZS system under the same damping and excitation, $\widetilde{Z}_e = 0.0449$ and $\beta = 0$. It can be seen that the proposed QZS system has a better vibration isolation performance than the conventional QZS system due to the construction of the device with two sets of symmetrically arranged precompressed tilting springs, which further optimizes the mechanical properties of the QZS system.

5. Dynamic Experiments of the QZS Device

Although considering the nonlinear coefficient of the tilted precompression springs can optimize the stiffness characteristics of the QZS system and thus improve the vibration isolation, the nonlinear springs are not readily available on the market, so we first manufactured the proposed device using linear springs to test and evaluate the vibration isolation performance of the QZS system, as shown in Figure 16(a). Figure 16(b) shows the device to remove the negative stiffness system and simulate the equivalent linear system with positive stiffness springs.

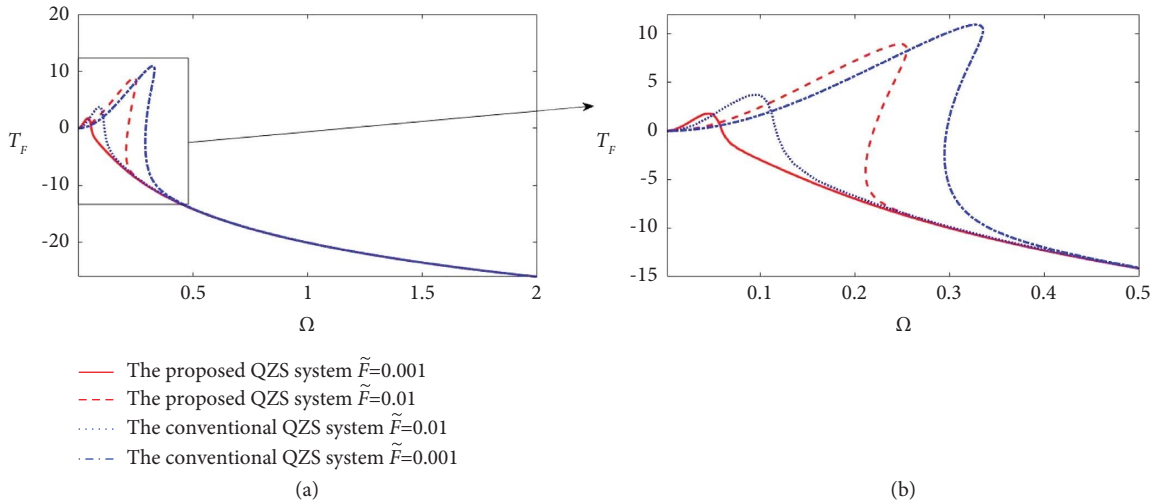

FIGURE 14: Force transmissibility of the proposed QZS system and the corresponding conventional QZS system with $\xi = 0.05$ and $\beta = 0$.

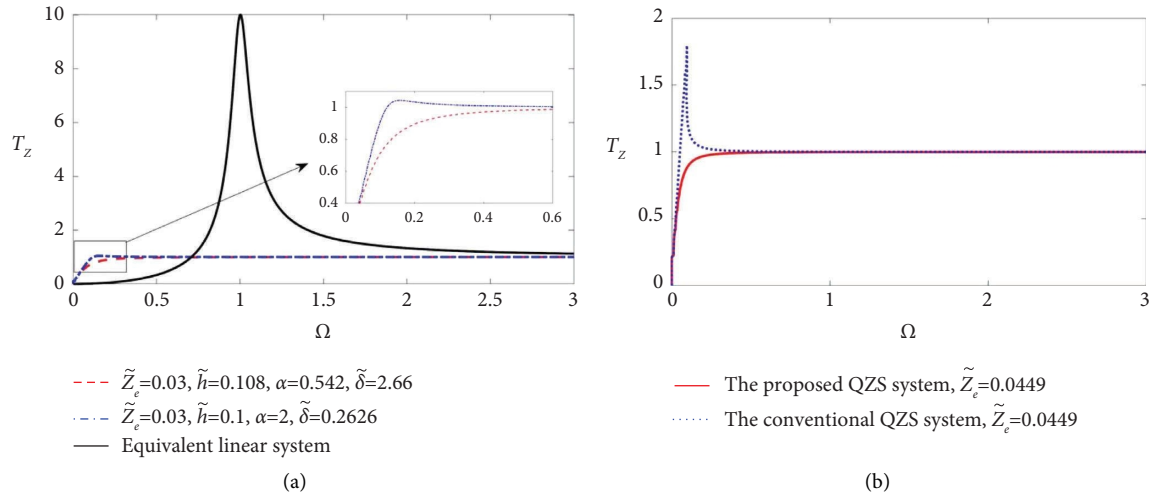

FIGURE 15: Relative displacement transmissibility of the proposed QZS system, the corresponding conventional QZS system, and the equivalent linear system: (a) $\xi = 0.05$, and $\beta \neq 0$ and (b) $\xi = 0.026$, $\beta = 0$, and $\widetilde{Z}_e = 0.0449$.

FIGURE 16: The QZS device and experimental model design: (a) the shaking table test of the QZS system: (1) the four degree of freedom shaking table, (2) the QZS device, (3) the isolated object, (4) four accelerometers, (5) INV-3602A signal acquisition system, and (6) computer for data acquisition and (b) the shaking table test of the equivalent linear system.

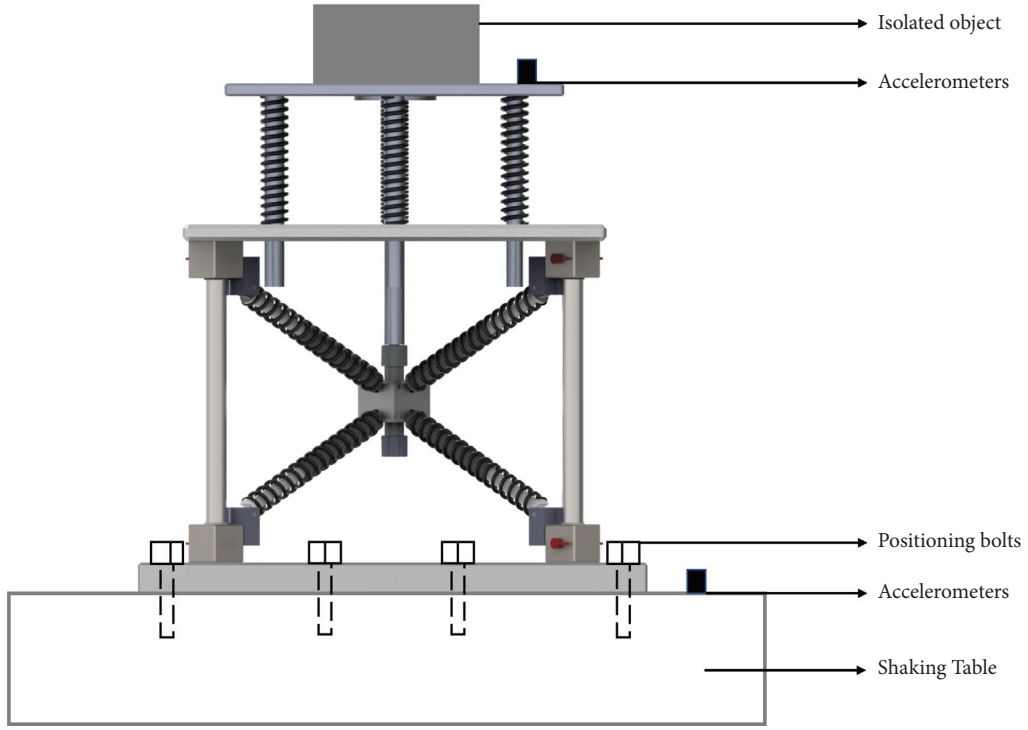

Figure 17: Frame diagram of the shaking table experiment platform.

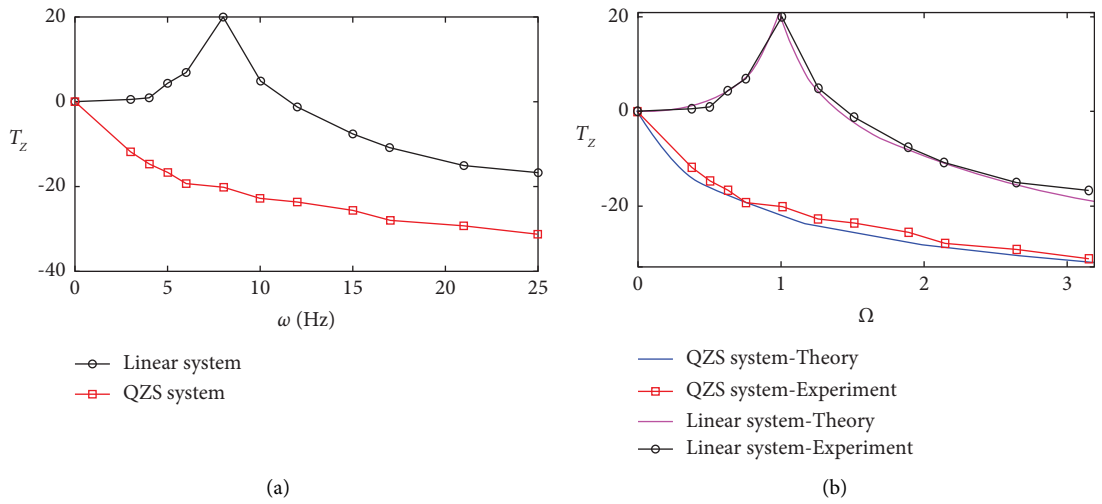

Figure 18: The experimental and theoretical displacement transmissibility curves of the QZS system and the equivalent linear system: (a) ω as the horizontal coordinate and (b) Ω as the horizontal coordinate.

The Frame diagram of the shaking table experiment platform is shown in Figure 17. The accelerometers are arranged on the shaking table and the isolated object, and the picked up acceleration signal is collected by the INV-3602A signal collector and subsequently processed by the Coinv DASP V10 software. To compare the vibration isolation performance of the QZS system and the equivalent linear system, displacement excitations were set in the frequency ranges of 3 Hz, 4 Hz, 5 Hz, 6 Hz, 8 Hz, 10 Hz, 12 Hz, 15 Hz, 17 Hz, 21 Hz, and 25 Hz, all with an excitation amplitude of 0.4 mm and a sampling frequency of 1024 Hz.

The root-mean-square value of the obtained time-domain displacement signal is used as the corresponding excitation amplitude and response amplitude, and the absolute displacement transmittance expressed in decibels (dB) is further obtained by the ratio of the two, as shown in Figure 18(a). The stiffness of the equivalent linear system in the experiment is $k_2 = 18572$ N/m, the load mass is 7.5 kg, and the resonant frequency can be obtained by $\omega_0 = (k_2/m)^{0.5}/2\pi = 7.92$ Hz. Based on the maximum value of the experimental displacement transmissibility of 19.95 dB, the damping ratio of the linear system can be obtained as $\xi = 0.045$, and the theoretical

displacement transmissibility of the equivalent linear system is further obtained, as shown in Figure 18(b).

The dimensionless vertical force in the dynamical analysis of the proposed QZS system uses $\widetilde{f} = 2.051\widetilde{x}^3$, which is obtained by fitting the restoring force curve under the experimental parameters. The experimental displacement excitation amplitude of 0.4 mm is dimensionlessly treated as $\widetilde{Z}_e = 0.00148$, and the theoretical displacement transmissibility of the QZS system can be further obtained, as shown in Figure 18(b).

When the harmonic excitation amplitude is 0.4 mm, the absolute displacement transmissibility of the QZS system has no peak value compared to the equivalent linear system and has a smaller vibration isolation starting frequency and a larger vibration isolation frequency range. The absolute displacement transmissibility shown in Figure 18 demonstrated the vibration isolation advantage of the proposed QZS system with respect to the equivalent linear system.

6. Conclusions

A new isolation device with spring systems has been proposed to improve vibration isolation performance by achieving quasi-zero-stiffness characteristics at the static equilibrium position and enlarge the QZS range through the optimal parameter design. The main conclusions are as follows:

(1) The static characteristics of the isolation device were theoretically studied for the proposed QZS system, and four sets of optimal stiffness curves are obtained by considering the nonlinear softening coefficient of the preloaded springs. These optimal stiffness curves can enlarge the QZS range and have lower dynamic stiffness in the entire compression stroke range.

(2) By analyzing the force and displacement transmissibility, the results show that (a) the QZS system with optimal parameters has a wider isolation frequency range and lower amplitude of vibration compared to the equivalent linear system and (b) the maximum value of relative transmissibility under harmonic excitation conditions disappears, which gives the QZS system with optimal parameters better low-frequency vibration isolation performance than the QZS system without considering the nonlinear coefficient and the equivalent linear system.

(3) The shaking table test demonstrated the vibration isolation advantage of the proposed QZS system with respect to the equivalent linear system by comparing and analyzing the experimental and theoretical absolute displacement transmissibility.

Data Availability

All data, models, or codes that support the findings of this study are available from the corresponding author upon reasonable request.

Conflicts of Interest

The authors declare that there are no conflicts of interest.

Authors' Contributions

All authors have contributed to the creation of this manuscript for important intellectual content and read and approved the final manuscript.

Acknowledgments

This research was financially supported by the authors.

References

[1] K. Chai, J. Lou, Q. Yang, and S. Liu, "Characteristic analysis of vibration isolation system based on high-static-low-dynamic stiffness," *Journal of Vibroengineering*, vol. 19, no. 6, pp. 4120–4137, 2017.

[2] F. Zhao, J. Ji, K. Ye, and Q. Luo, "An innovative quasi-zero-stiffness isolator with three pairs of oblique springs," *International Journal of Mechanical Sciences*, vol. 192, Article ID 106093, 2021.

[3] F. Zhao, J. C. Ji, K. Ye, and Q. Luo, "Increase of quasi-zero-stiffness region using two pairs of oblique springs," *Mechanical Systems and Signal Processing*, vol. 144, Article ID 106975, 2020.

[4] F. Zhao, J. Ji, Q. Luo, S. Cao, L. Chen, and W. Du, "An improved quasi-zero-stiffness isolator with two pairs of oblique springs to increase isolation frequency band," *Nonlinear Dynamics*, vol. 104, no. 1, pp. 349–365, 2021.

[5] Z. Hao and Q. Cao, "The isolation characteristics of an archetypal dynamical model with stable-quasi-zero-stiffness," *Journal of Sound and Vibration*, vol. 340, pp. 61–79, 2015.

[6] F. Niu, L. Meng, W. Wu et al., "Design and analysis of a quasi-zero-stiffness isolator using a slotted conical disk spring as negative stiffness structure," *Journal of Vibroengineering*, vol. 16, no. 4, pp. 1769–1785, 2014.

[7] A. R. Valeev, A. N. Zotov, and S. A. Kharisov, "Application of disk springs for manufacturing vibration isolators with quasi-zero-stiffness," *Chemical and Petroleum Engineering*, vol. 51, no. 3-4, pp. 194–200, 2015.

[8] P. Chen and Y. Zhou, "Experiment and numerical investigations on a vertical isolation system with quasi-zero-stiffness property," in *Vibration Engineering for a Sustainable Future: Active and Passive Noise and Vibration Control,*Vol. 1, Springer International Publishing, Berlin, Germany, 2020.

[9] C. Liu and K. Yu, "Design and experimental study of a quasi-zero-stiffness vibration isolator incorporating transverse groove springs," *Archives of Civil and Mechanical Engineering*, vol. 20, no. 3, pp. 67–21, 2020.

[10] K. Ye and J. C. Ji, "An origami inspired quasi-zero-stiffness vibration isolator using a novel truss-spring based stack Miura-ori structure," *Mechanical Systems and Signal Processing*, vol. 165, Article ID 108383, 2022.

[11] H. Han, V. Sorokin, L. Tang, and D. Cao, "A nonlinear vibration isolator with quasi-zero-stiffness inspired by Miura-origami tube," *Nonlinear Dynamics*, vol. 105, no. 2, pp. 1313–1325, 2021.

[12] X. Yang, J. Zheng, J. Xu, W. Li, Y. Wang, and M. Fan, "Structural design and isolation characteristic analysis of new quasi-zero-stiffness," *Journal of vibration engineering & technologies*, vol. 8, no. 1, pp. 47–58, 2020.

[13] L. Kashdan, C. Conner Seepersad, M. Haberman, and P. S. Wilson, "Design, fabrication, and evaluation of negative stiffness elements using SLS," *Rapid Prototyping Journal*, vol. 18, no. 3, pp. 194–200, 2012.

[14] X. Liu, X. Huang, and H. Hua, "On the characteristics of a quasi-zero-stiffness isolator using Euler buckled beam as negative stiffness corrector," *Journal of Sound and Vibration*, vol. 332, no. 14, pp. 3359–3376, 2013.

[15] X. Liu, Q. Zhao, Z. Zhang, and X. Zhou, "An experiment investigation on the effect of Coulomb friction on the displacement transmissibility of a quasi-zero-stiffness isolator," *Journal of Mechanical Science and Technology*, vol. 33, no. 1, pp. 121–127, 2019.

[16] J. Kim, Y. Jeon, S. Um, U. Park, K. S. Kim, and S. Kim, "A novel passive quasi-zero-stiffness isolator for ultra-precision measurement systems," *International Journal of Precision Engineering and Manufacturing*, vol. 20, no. 9, pp. 1573–1580, 2019.

[17] D. Zou, G. Liu, Z. Rao, T. Tan, W. Zhang, and W. H. Liao, "A device capable of customizing nonlinear forces for vibration energy harvesting, vibration isolation, and nonlinear energy sink," *Mechanical Systems and Signal Processing*, vol. 147, Article ID 107101, 2021.

[18] G. Gatti, "An adjustable device to adaptively realise diverse nonlinear force-displacement characteristics," *Mechanical Systems and Signal Processing*, vol. 180, Article ID 109379, 2022.

[19] M. Sun, G. Song, Y. Li, and Z. Huang, "Effect of negative stiffness mechanism in a vibration isolator with asymmetric and high-static-low-dynamic stiffness," *Mechanical Systems and Signal Processing*, vol. 124, pp. 388–407, 2019.

[20] Y. Shan, W. Wu, and X. Chen, "Design of a miniaturized pneumatic vibration isolator with high-static-low-dynamic stiffness," *Journal of Vibration and Acoustics*, vol. 137, no. 4, 2015.

[21] B. Yan, H. Ma, C. Zhao, C. Wu, K. Wang, and P. Wang, "A vari-stiffness nonlinear isolator with magnetic effects: theoretical modeling and experimental verification," *International Journal of Mechanical Sciences*, vol. 148, pp. 745–755, 2018.

[22] H. Ma and B. Yan, "Nonlinear damping and mass effects of electromagnetic shunt damping for enhanced nonlinear vibration isolation," *Mechanical Systems and Signal Processing*, vol. 146, Article ID 107010, 2021.

[23] H. Dai, X. Jing, Y. Wang, X. Yue, and J. Yuan, "Post-capture vibration suppression of spacecraft via a bio-inspired isolation system," *Mechanical Systems and Signal Processing*, vol. 105, pp. 214–240, 2018.

[24] Y. Wang, X. Jing, and Y. Guo, "Nonlinear analysis of a bio-inspired vertically asymmetric isolation system under different structural constraints," *Nonlinear Dynamics*, vol. 95, no. 1, pp. 445–464, 2019.

[25] G. Yan, S. Wang, H. Zou, L. Zhao, Q. Gao, and W. Zhang, "Bio-inspired polygonal skeleton structure for vibration isolation: design, modelling, and experiment," *Science China Technological Sciences*, vol. 63, no. 12, pp. 2617–2630, 2020.

[26] R. S. Lakes, "Extreme damping in compliant composites with a negative-stiffness phase," *Philosophical Magazine Letters*, vol. 81, no. 2, pp. 95–100, 2001.

[27] R. S. Lakes, T. Lee, A. Bersie, and Y. C. Wang, "Extreme damping in composite materials with negative-stiffness inclusions," *Nature*, vol. 410, no. 6828, pp. 565–567, 2001.

[28] W. J. Drugan, "Elastic composite materials having a negative stiffness phase can be stable," *Physical Review Letters*, vol. 98, no. 5, Article ID 055502, 2007.

[29] Q. Cao, M. Wiercigroch, E. E. Pavlovskaia, C. Grebogi, and J. M. T Thompson, "Archetypal oscillator for smooth and discontinuous dynamics," *Physical Review*, vol. 74, no. 4, Article ID 046218, 2006.

[30] Q. J. Cao, Y. W. Han, T. W. Liang, M. Wiercigroch, and S. Piskarev, "Multiple buckling and codimension-three bifurcation phenomena of a nonlinear oscillator," *International Journal of Bifurcation and Chaos*, vol. 24, no. 1, Article ID 1430005, 2014.

[31] W. G. Molyneux, *Supports for Vibration Isolation*, Cranfield University, Cranfield, United Kingdom, 1957.

[32] A. Carrella, M. J. Brennan, and T. P. Waters, "Static analysis of a passive vibration isolator with quasi-zero-stiffness characteristic," *Journal of Sound and Vibration*, vol. 301, no. 3-5, pp. 678–689, 2007.

[33] A. Carrella, M. J. Brennan, I. Kovacic, and T. P. Waters, "On the force transmissibility of a vibration isolator with quasi-zero-stiffness," *Journal of Sound and Vibration*, vol. 322, no. 4-5, pp. 707–717, 2009.

[34] A. Carrella, M. J. Brennan, T. P. Waters, and V. Lopes, "Force and displacement transmissibility of a nonlinear isolator with high-static-low-dynamic-stiffness," *International Journal of Mechanical Sciences*, vol. 55, no. 1, pp. 22–29, 2012.

[35] A. Carrella, M. I. Friswell, A. Zotov, D. J. Ewins, and A. Tichonov, "Using nonlinear springs to reduce the whirling of a rotating shaft," *Mechanical Systems and Signal Processing*, vol. 23, no. 7, pp. 2228–2235, 2009.

[36] S. A. Neild and D. J. Wagg, "Applying the method of normal forms to second-order nonlinear vibration problems," *Proceedings of the Royal Society A: Mathematical, Physical and Engineering Sciences*, vol. 467, no. 2128, pp. 1141–1163, 2011.

[37] D. Wagg and L. Virgin, *Exploiting Nonlinear Behavior in Structural Dynamics*, Vol. 536, Springer Science & Business Media, Berlin, Germany, 2012.

[38] A. D. Shaw, S. A. Neild, and D. J. Wagg, "Dynamic analysis of high static low dynamic stiffness vibration isolation mounts," *Journal of Sound and Vibration*, vol. 332, no. 6, pp. 1437–1455, 2013.

[39] T. Yang and Q. Cao, "Delay-controlled primary and stochastic resonances of the SD oscillator with stiffness nonlinearities," *Mechanical Systems and Signal Processing*, vol. 103, pp. 216–235, 2018.

[40] T. Yang and Q. Cao, "Noise-and delay-enhanced stability in a nonlinear isolation system," *International Journal of Nonlinear Mechanics*, vol. 110, pp. 81–93, 2019.

[41] T. Yang and Q. Cao, "Nonlinear transition dynamics in a time-delayed vibration isolator under combined harmonic and stochastic excitations," *Journal of Statistical Mechanics: Theory and Experiment*, vol. 2017, no. 4, Article ID 043202, 2017.

[42] I. Kovacic, M. J. Brennan, and T. P. Waters, "A study of a nonlinear vibration isolator with a quasi-zero-stiffness characteristic," *Journal of Sound and Vibration*, vol. 315, no. 3, pp. 700–711, 2008.